Supporting Information

Disentangling electron-phonon coupling and thermal expansion effects in the bandgap renormalization of perovskite nanocrystals

Andrea Rubino[1], Adrián Francisco-López[2], Alex Barker[3], Annamaria Petrozza[3], Mauricio E. Calvo[1], Alejandro R. Goñi[2,4], Hernán Míguez[1]

[1]Institute of Materials Science of Seville, Spanish National Research Council-University of Seville, C/Américo Vespucio 49, 41092, Seville, Spain.

[2]Institut de Ciència de Materials de Barcelona, ICMAB-CSIC, Campus UAB, 08193 Bellaterra, Spain.

[3]Instituto Italiano di Tecnologia, CNST, Milano.

[4]ICREA, Passeig Lluís Companys 23, 08010 Barcelona, Spain.

Methods

Sample preparation

$MAPbI_3$ nanocrystal synthesis consists of a one-step process already reported elsewhere [1]. The method involves the preparation, at room temperature, of a solution of the perovskites precursors (MAI + $PbCl_2$), in a molar ratio of 3 to 1, in dimethylformamide (DMF). The solution is then deposited by spin coating on a 1-μm thick porous layer composed of 30 nm silica nanoparticles. In this way, the precursors can diffuse through the empty spaces between the silica particles and, with subsequent heat treatment the perovskite crystallizes in the accessible voids. In the case of $MAPbI_3$ bulk films, the solution is directly deposited on a glass substrate previously cleaned with oxygen plasma. Preparing nanocrystals of different sizes is carried out by diluting the

precursor solution at different concentrations. Previously, the porous silica matrix is obtained by repeated dip coating deposition of a colloidal dispersion of the SiO_2 nanoparticles (Ludox, 34% in water). The stratification of these nanoparticles, up to a thickness of about 1 micron, provides a matrix with a porosity of 40% and pore diameters of 12-16 nm. The preparation of the porous silica films was carried out in a chamber with humidity control, whereas the synthesis of the perovskite nanocrystals was performed in a glovebox. The stratification observed in Fig. 1a in the main body of the manuscript results from the successive dip-coating depositions of the silica particles that form the matrix.

The structural characterization was conducted using a FEI Talos F200S scanning/transmission electron microscope and a D8C diffractometer. In the first case, the $MAPbI_3$-SiO_2 composite films were deposited on silicon substrates and by means of a focused ion beam (FIB, Carl Zeiss Auriga) the lamellae were obtained for TEM. For the XRD measurements the acquisition of the data was taken between 130 K and 300 K in the 10º-50º 2θ-angle range.

Transmission electron microscopy (TEM) analysis

Cross sections of a few of the infiltrated porous SiO_2 matrices, i.e. already containing nanocrystals (NCs), were prepared by the focused ion beam (FIB) technique for their subsequent morphological study using transmission electron microscopy (TEM) and high-resolution TEM (HRTEM). A representative example is shown in Fig. S1 and S2, corresponding to a sample with a concentration of the perovskite precursors of 20 wt% [1]. Here heavier atoms like Pb and I of the perovskite NCs appear darker in HRTEM; lighter atoms like Si and O of the silica matrix appear thus as brighter areas. In the high-resolution image, one can infer that the rough estimates of the average NC size, obtained from the PL peak positions at room temperature using Eq. (2) of the main manuscript, are of the right order of magnitude (below ca. 10 nm in diameter). A histogram that represents the statistical diameter size obtained from the image is shown as an inset of Figure S2

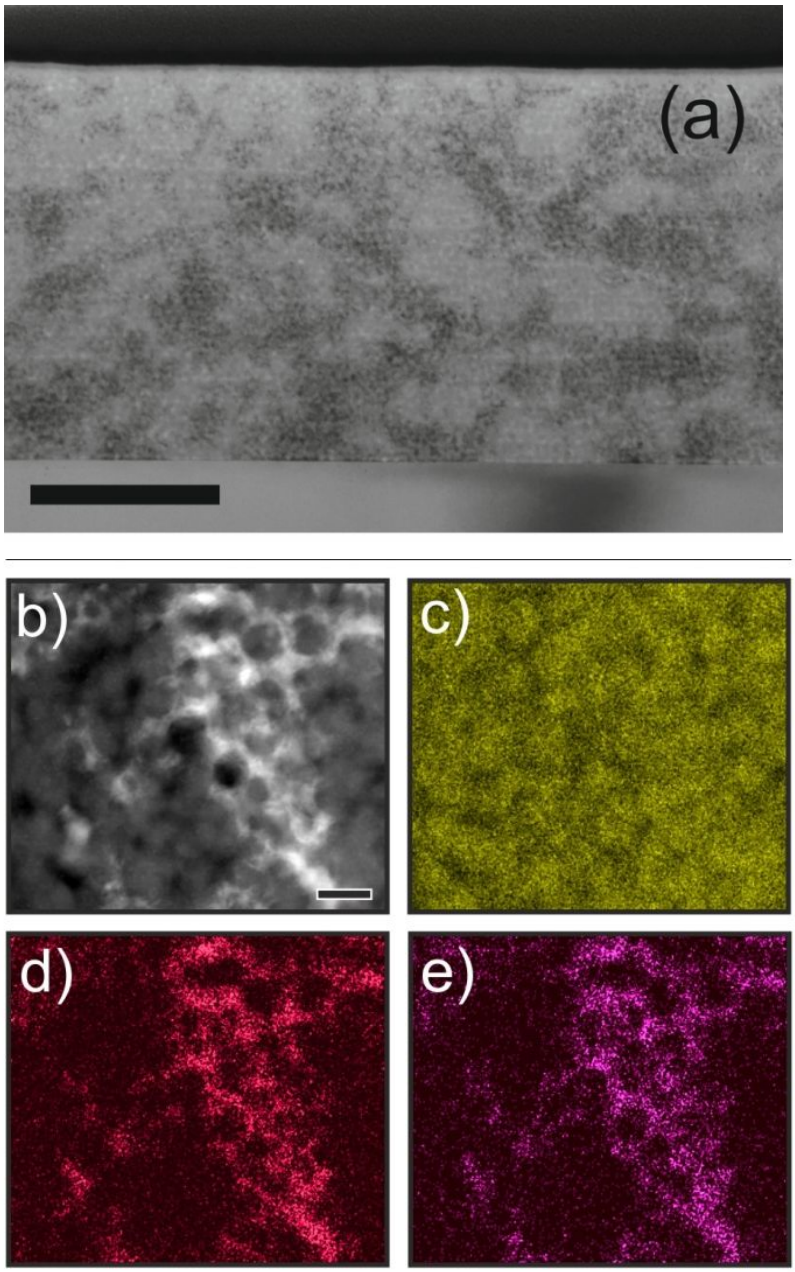

Figure S1: (a) TEM image of a FIB cross-section of a porous SiO_2 layer infiltrated with $MAPbI_3$ perovskite precursors at 20 wt% (average NC size is 8 nm in diameter). Scale bar represents 500 nm. (b) High-resolution TEM cross section of the same sample shown in panel (a). Scale bar is 50 nm. From (c) to (e), EDX mappings of the same area presented in (b) for (c) Si, (d) I, and (e) Pb.

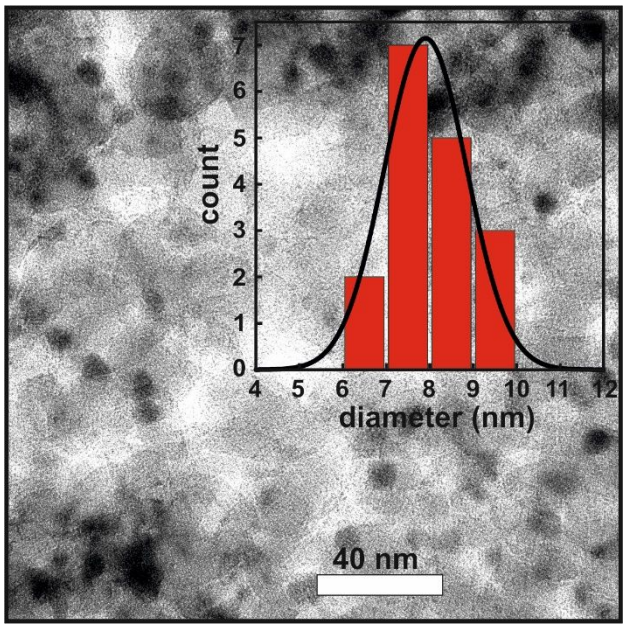

Figure S2: HRTEM image of a portion of the cross-section shown in fig S1a. In the inset the estimated NC size distribution, comparable to the diameter obtained from the PL peak positions at room temperature using Eq. (2) of the main manuscript (ca. 8 nm).

X-ray diffraction (XRD) analysis

A structural study of the temperature-induced phase transition of $MAPbI_3$ bulk (thin film) and the nanocrystals was performed by X-ray diffraction in the temperature range between 130 K and 300 K. The XRD results are displayed in Figs. S3 to S7. In the zoomed images (Fig. S4) of the thin-film XRD patterns, the diffraction peaks exhibit a shift to larger 2θ values as a consequence of the contraction of the lattice when temperature decreases. The diffraction patterns of the thin film also show peaks corresponding to the orthorhombic phase at 14.4, 23.0 and 33.0 degrees (Figs. S4a, b, d) [2]. These peaks survive up to a temperature of 150 K.

Regarding the nanocrystals synthesized in the silica nanoparticle matrix, there are several technical complications that deserve consideration. First of all, there is a strong diffraction peak at around 25 degrees, which corresponds to the silica that overwhelms the signal from the perovskite. Considering the scarce quantity of perovskite material, only the results for the most concentrated samples (NCs 20%) are reliable. In addition, the presence of water molecules absorbed in the pores of the matrix leads to ice formation by crystallization at low temperatures. Unfortunately, the diffraction peaks of ice overlap with those of the perovskites in the ranges around 23 and 33 degrees (Fig. S5). The zoomed images of the XRD patterns of a $MAPbI_3$ NCs 20% sample are shown in Fig. S6. In this composite samples, the low amount of nanocrystals in the SiO_2 layer together with the reduced size of the nanocrystals, demands higher integration times to obtain clear signals in the diffractograms. Thus, the XRD measurements of the NC samples were performed solely for four temperatures. In the case of the NCs 20% sample, it is particularly interesting to analyse the peak at 14 degrees. This peak presents two typical contributions which are ascribed to the orthorhombic phase of $MAPbI_3$, which are observable up to a temperature of 170 K. This would confirm the hypothesis that the phase transition is moving up in temperature as compared to bulk.

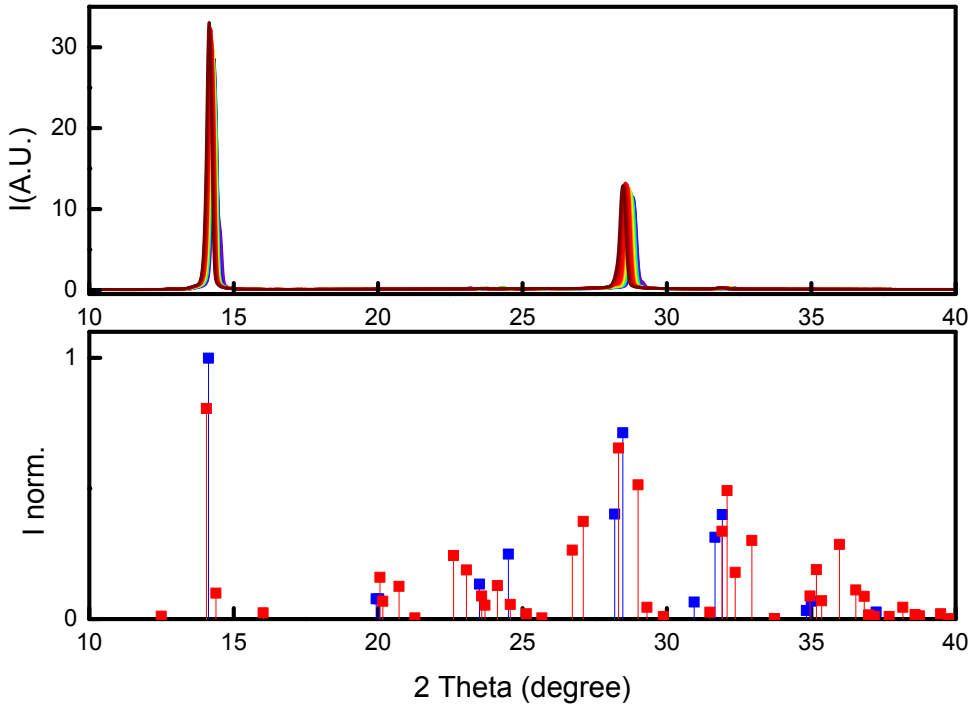

Figure S3: Upper panel: XRD of a $MAPbI_3$ bulk film recorded at different temperatures from 130 K (violet line) to 300 K (red line) every 10 K. Bottom panel: Simulated XRD patterns (at 25 ºC) for $MAPbI_3$ tetragonal (blue line) and orthorhombic (red line) phases.

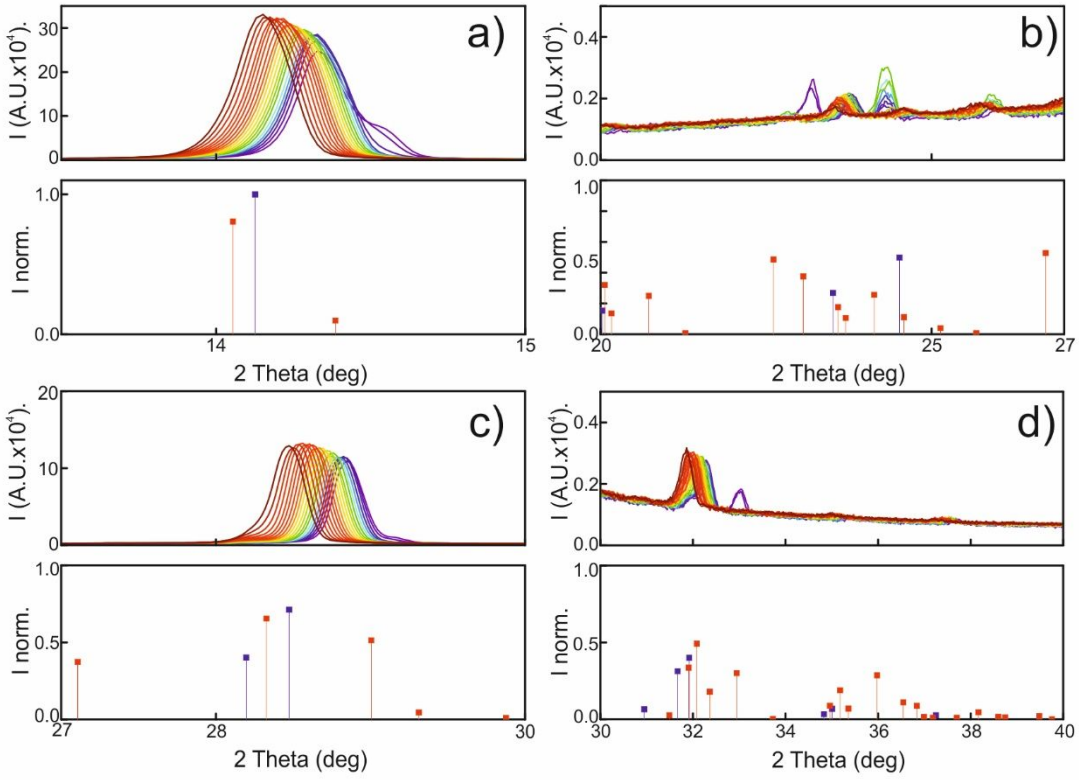

Figure S4: Selected regions of the XRD patterns of Fig. S3 for different 2θ ranges: (a) 10 <2θ<18 degrees; (b) 20<2θ<27 degrees (c) 27<2θ<30 degrees; (d) 30<2<40 degrees.

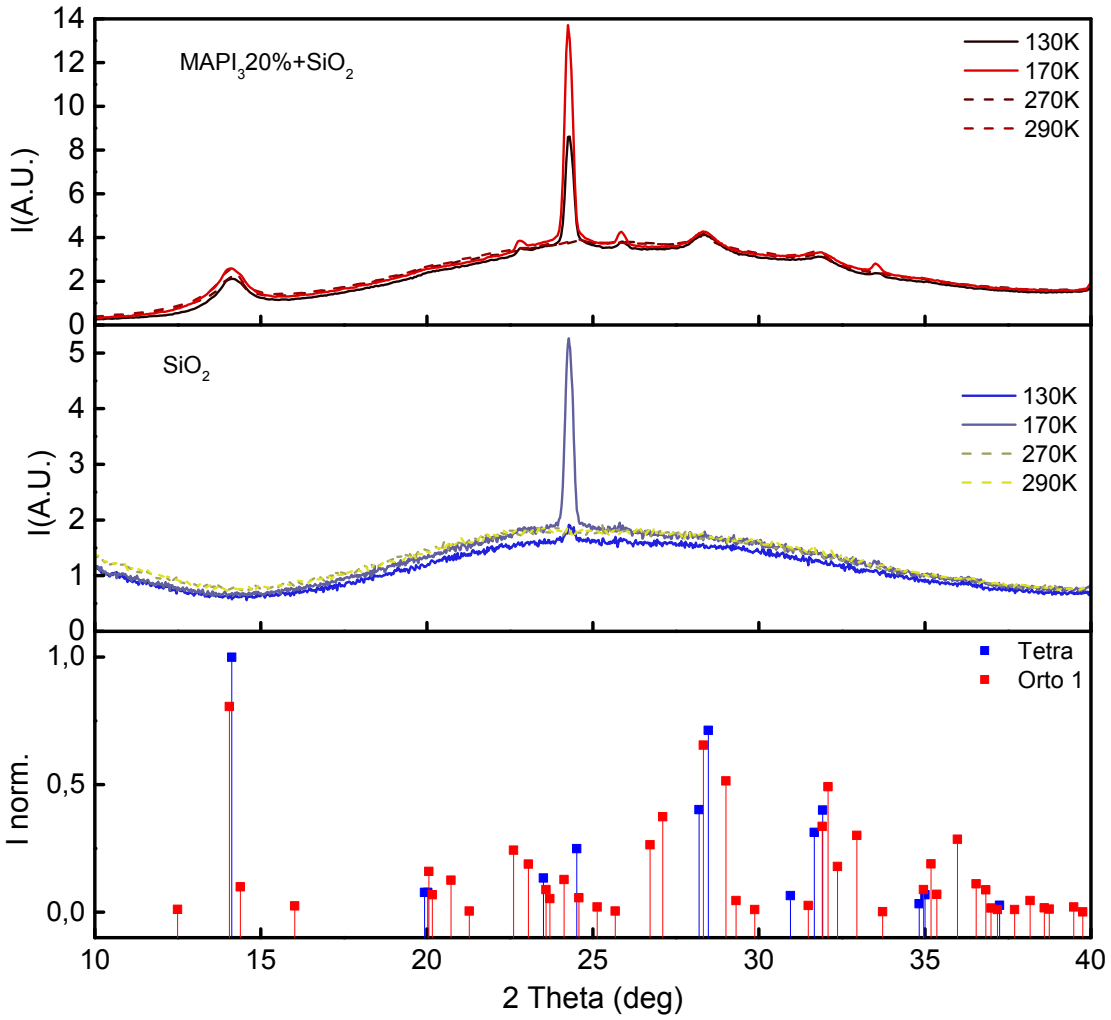

Figure S5: Upper panel: XRD patterns of a $MAPbI_3$ NCs 20% sample with the nanocrystals embedded in the SiO_2 mesoporous scaffold measured at four different temperatures. Middle panel: XRD patterns of the empty SiO_2 scaffold obtained at the same temperatures than the NCs 20% sample. Lower panel: Simulated XRD patterns of the tetragonal (blue line) and orthorhombic (red line) phases of $MAPbI_3$. The strong peak at $2\theta \cong 24$ degrees belong to solid water.

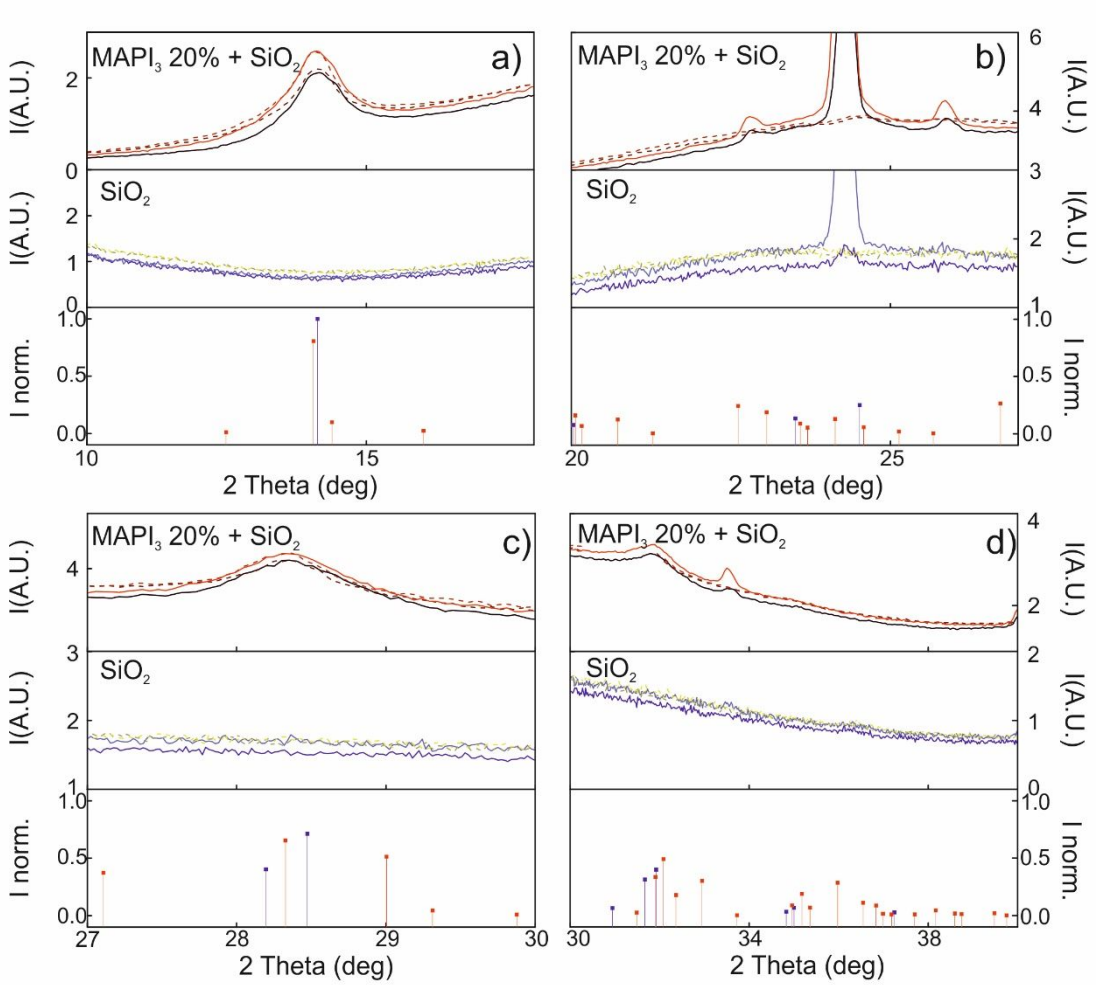

Figure S6: Selected regions of the XRD patterns of Fig. S5 for different 2θ ranges: (a) $10<2\theta<18$ degrees; (b) $20<2\theta<27$ degrees (c) $27<2\theta<30$ degrees; (d) $30<2\theta<40$ degrees.

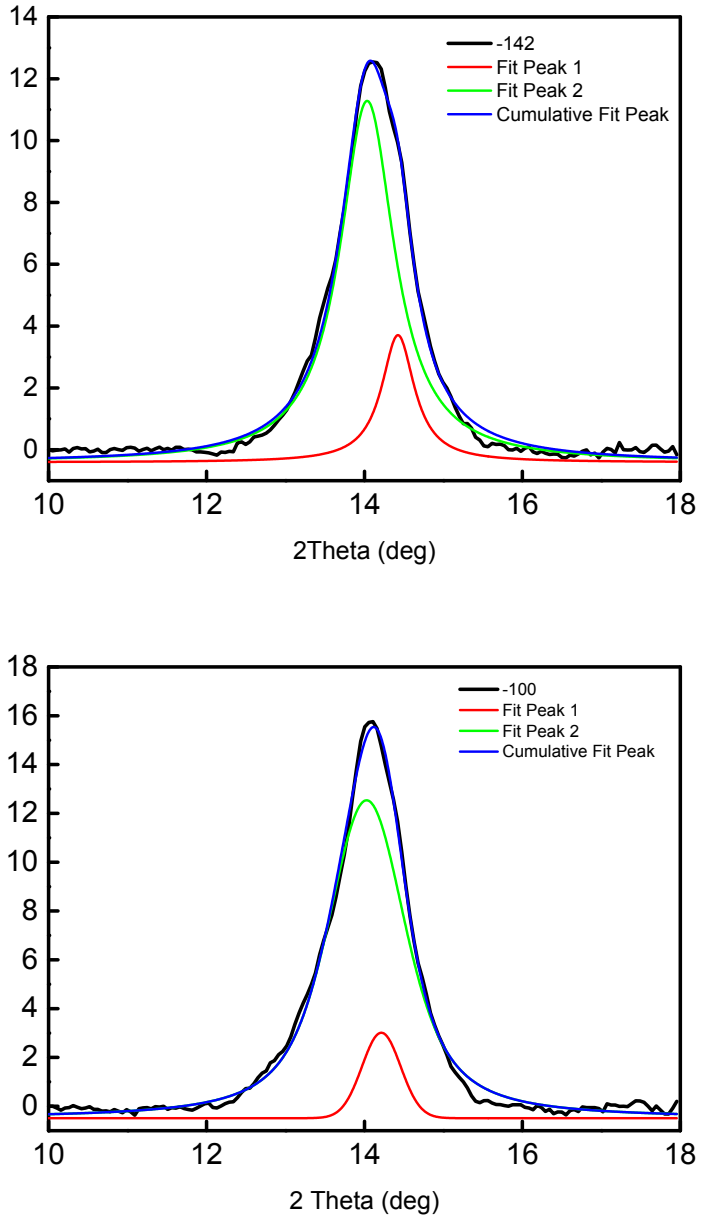

Figure S7: Analysis of the diffraction peak at 14 degrees presented in the XRD pattern from Fig. S6a. The peak presents a double-peak structure typical of the orthorhombic phase at both temperatures (a) 130 K and (b) 170 K.

Temperature-dependent Raman scattering

Further structural information about the NC samples can be gained from Raman scattering measurements performed as a function of temperature. Figure S8 shows series of Raman spectra of MAPbI3 bulk (single crystal) and a NCs 3% sample recorded in a wide temperature range above 80 K using infrared (785 nm) excitation. The changes in line shape are interpreted in terms of the occurrence of the tetragonal-to-orthorhombic phase transition in $MAPbI_3$ [3,4]. As shown in Fig. S8a for the bulk material, at this phase transition the Raman spectra of $MAPbI_3$ exhibit a pronounced reduction of the line width of the phonon modes of the inorganic cage [3]. This is a direct consequence of the locking of the organic cations in the cage voids due to the reduced volume and symmetry of the orthorhombic unit cell. The Raman spectra of the NCs 3% sample measured at different temperatures between ambient and 80 K (see Fig. S8b) seem to indicate a change in line shape below 170 K and a clear sharpening of the Raman peaks at around 100 K. Nevertheless, the peak-width reduction in the NCs is by far less marked as for the bulk [3]. We thus infer that in the NCs the locking of the MA molecules is not complete, probably indicating partial transformation from tetragonal to orthorhombic, i.e., there must exist certain degree of phase coexistence even at such a low temperature like 80 K.

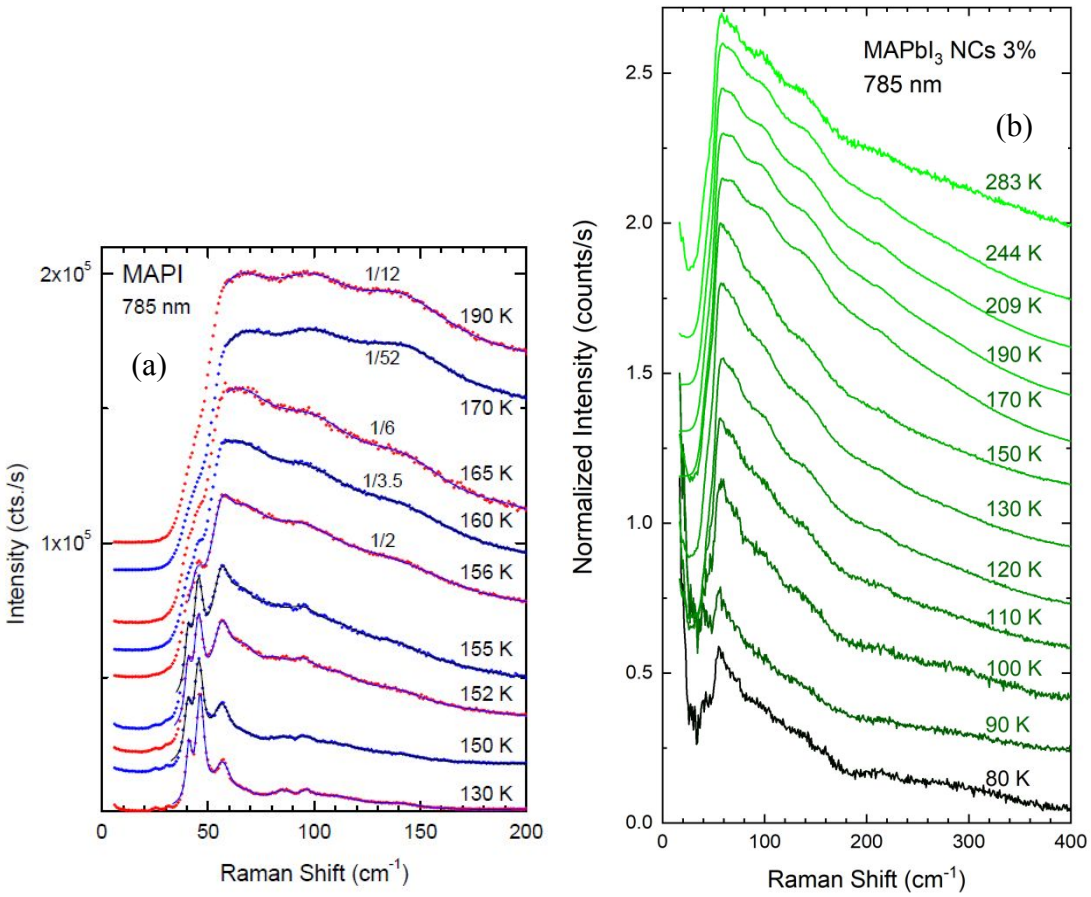

Figure S8: Raman spectra of (a) a $MAPbI_3$ single crystal and (b) a NCs 3% sample (average NC diameter of 4 nm) measured at different temperatures in the spectral range of the inorganic cage phonon modes.

On the excitonic character of the PL emission

Excitons, by definition, are quasi-particles composed by an electron-hole pair correlated by mutual Coulomb attraction. The Coulomb interaction presents two key features: despite being screened by the dielectric environment, it is extremely long ranged, and it cannot be shut off. For a typical bulk semiconductor material, the Coulomb interaction is strongly screened via the large dielectric function. As a result, electrons and holes are weakly bound forming the so-called Wannier excitons [5]. The energy spectrum corresponding to the relative motion of the two particles about the center of mass resembles that of the hydrogen atom: There is a series of bound states with energies below the gap and continuum states above the gap. In the continuum states, the exciton is ionized but the electron and hole are strictly speaking not free, because their wave function is modified by the Coulomb attraction rather than being a plane wave. This might be irrelevant as far as the transport properties of the material are concerned, because once the charges are separated and collected by the electrodes, the residual Coulomb interaction plays no role at all. For all practical purposes the carriers can be considered free in terms of their transport properties. However, this is not the case for the optical absorption. Even if the peak-like features corresponding to the discrete-state absorption are absent (bound states become thermally ionized when k_BT exceeds the exciton binding energy), the exciton continuum leads to a step-like absorption edge, in frank contrast with the square-root-like line shape of the free carrier case. At its onset, the absorption is strongly enhanced by excitonic effects [6,7]. First important conclusion: *The absence of an absorption peak due to the thermal ionization of the bound-exciton ground state does not mean that the optical absorption lacks excitonic character.*

For the optical emission the situation is slightly different. After photo-excitation, the photo-generated electrons and holes relax their excess energy by non-radiative relaxation processes (mainly via electron-phonon interaction), approaching the bottom of the conduction band and top of the valence band, respectively. Yet the carriers are correlated by Coulomb interaction (it is long-ranged and cannot be switched off). The luminescence quantum yield is simply given by:

$$Q = \frac{\frac{1}{\tau_R}}{\frac{1}{\tau_R} + \frac{1}{\tau_{NR}}} \qquad \text{(S1)}$$

Here is τ_R and τ_{NR} the radiative recombination time and the non-radiative relaxation time, respectively. In good quality crystals, the non-radiative relaxation times of the excited states are always shorter than that of the ground state. As a consequence, PL emission always proceeds from the lowest-energy states [8]. For the excitonic case this means that thermal dissociation cannot hinder bound exciton states to play a main role in emission because their optical recombination is favored against that of continuum states due to the much shorter lifetime of the latter. Second important conclusion: *Even at high temperatures compared with the exciton binding energy, the PL emission is dominated by the radiative recombination of the bound–exciton ground state.*

In contrast, for nano-crystals the excitonic character of the optical emission is just undeniable. This is simply because quantum confinement causes the collapse of the whole continuum spectrum into a series of discrete energy levels, which, of course, are influenced by the Coulomb interaction between the confined particles. Electrons and holes in NCs are always correlated by their mutual Coulomb attraction, i.e. forming bound-exciton states irrespective of the temperature. The relative importance of the confining potential as compared with the strength of the Coulomb attraction is determined by the ratio of the NC size to the extension of the exciton wave function. The latter is approx. given by the exciton Bohr radius of the free exciton (unconfined, bulk case). Third important conclusion: *Confinement effects become pronounced for smaller NC sizes than the Bohr radius in the bulk*.

Estimation of nanocrystal size employing Brus formula

The blue-shift observed in Figure 2a is clear evidence of quantum confinement effects, which can be roughly accounted for using the equation derived by L. E. Brus for the energy of the optical transition between electron and hole ground-states, accounting for excitonic effects, in a spherical semiconductor nanocrystal of radius R:[9]

$$E_g = E_{g,bulk} + \frac{h^2}{8\mu R^2} - \frac{1.8\, e^2}{4\pi\varepsilon_0\varepsilon_r R} \qquad \text{(S2)}$$

where $E_{g,bulk}$ is the band-gap energy of $MAPbI_3$ bulk (1.59 eV in our case), h is Planck's constant, μ is the exciton reduced mass, e is the electron charge, and ε_0 and ε_r are the vacuum permittivity and the dielectric constant of $MAPbI_3$, respectively. Using, in Eq. (2), an exciton reduced mass of 0.3 m_0,[10] where m_0 is the electron mass, and a dielectric constant of 17,[11] we estimated that our $MAPbI_3$ NC diameters are ranging from 4 nm to 8 nm. This range coincides well with the result of the electron microscopy analysis for the case of larger crystals (see Figure 1b and S2), thus, the calculated diameters, including the smaller crystals, were used to build the top x-axis of Figure 2a. We note that despite the approximate nature of the estimates due to several assumptions contained in Eq. (S2) (i.e., spherical shape, quasi-infinite potential well, parabolic bands, constant effective mass, etc.), the NC *diameters* obtained from Brus equation are in good agreement with the experimental observations performed by electron microscopy. Wannier excitons in bulk are delocalized, i.e., they move freely through the crystal, but their energy spectrum corresponding to the radial coordinate relative to the center-of-mass resembles that of the hydrogen atom.**Error! Bookmark not defined.** The exciton binding energy E_b and exciton Bohr radius a_B are given in terms of the hydrogen atom magnitudes as:

$$E_b = \frac{\mu}{m_0 \cdot \varepsilon_r^2} \cdot \mathcal{R}_H \qquad with\ \mathcal{R}_H = 13.605\ eV \qquad \text{(S3)}$$

$$a_B = \frac{m_0 \cdot \varepsilon_r}{\mu} \cdot a_H \qquad with\ a_H = 0.05292\ nm \qquad \text{(S4)}$$

Using the values of the exciton reduced mass and dielectric constant cited before when evaluating Eq. (S2), we obtain an exciton binding energy of 14 meV (fully in agreement with the consensus value of 15 meV of the literature, please see refs. 44-46 in the main body of the manuscript) and a Bohr radius of 3 nm.

.

Temperature-dependent PL measurements

The temperature-dependent PL measurements were carried out using a homemade setup and a 450 nm laser for excitation in combination with a liquid-nitrogen flow cryostat. The high-pressure PL measurements were performed at room temperature employing a gasketed diamond anvil cell (DAC). Silicon oil was used as pressure transmitting medium, which ensures good hydrostatic conditions and proved to be chemically inert to the $MAPbI_3$ NCs. The composite $MAPbI_3$-SiO_2 film was scraped from the glass substrate with a sharp knife and a fine powder was placed in the DAC together with a ruby sphere for pressure calibration [12]. The PL spectra were excited with the 633 nm line of a He−Ne laser. In all cases, a very low incident light power density below 15 W/cm^2 was used to avoid any photo-degradation of the samples, such that thermal damage by the laser can be safely ruled out. Spectra were collected using a 20× long working distance objective with NA = 0.35 and dispersed with a high-resolution LabRam HR800 grating spectrometer equipped with a charge-coupled device detector. PL spectra were corrected for the spectral response of the spectrometer by normalizing each spectrum using the detector and the 600 grooves/mm grating characteristics.

Figure S9 collects the spectra of PL used to compose the color maps shown in figure 2(b-e) of the main text whereas Figure S10 shows representative PL spectra recorded at 140 K for different nanostructured $MAPbI_3$ samples, as indicated, to illustrate the line shape analysis of the PL profiles. Different colors correspond to the main free-exciton peak (green shaded) and an auxiliary peak (blue shaded) used to improve the fit. For the line-shape fitting of the PL spectra we used a Gaussian-Lorentzian cross-product function. Its expression reads as [4,13]:

$$G \times L(E) = A \cdot exp\left(-4 \cdot ln2 \cdot \frac{(1-s)\cdot(E_0-E)^2}{\Gamma^2} \right) \cdot \frac{\Gamma^2}{4\cdot s\cdot(E_0-E)^2+\Gamma^2} \quad \text{(S3)}$$

where A is the amplitude prefactor, E_0 and E are the peak energy position and photon energy, respectively, Γ is the half width at half maximum (HWHM) and s is a weight parameter which takes the value s = 0 for pure Gaussian line shape and s = 1 for pure Lorentzian. The values of these four adjustable parameters were obtained as a function of temperature from line shape fits to the measured PL spectra using Eq. (3), as exemplified in Fig.S10 [14].

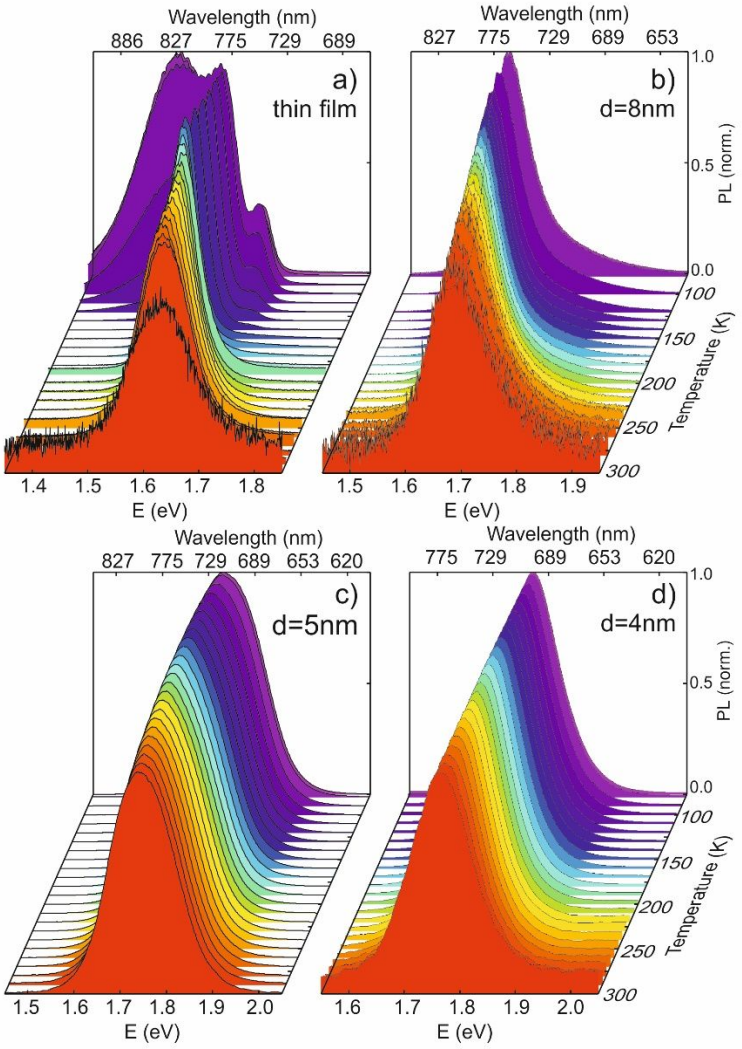

Figure S9: (a-d) Cascade of normalized PL spectra recorded at different temperatures from 80 K to 300 K for (a) thin film and the NCs embedded in a silica matrix corresponding to average NC sizes of (b) 8 nm, (c) 5 nm, and (d) 4 nm

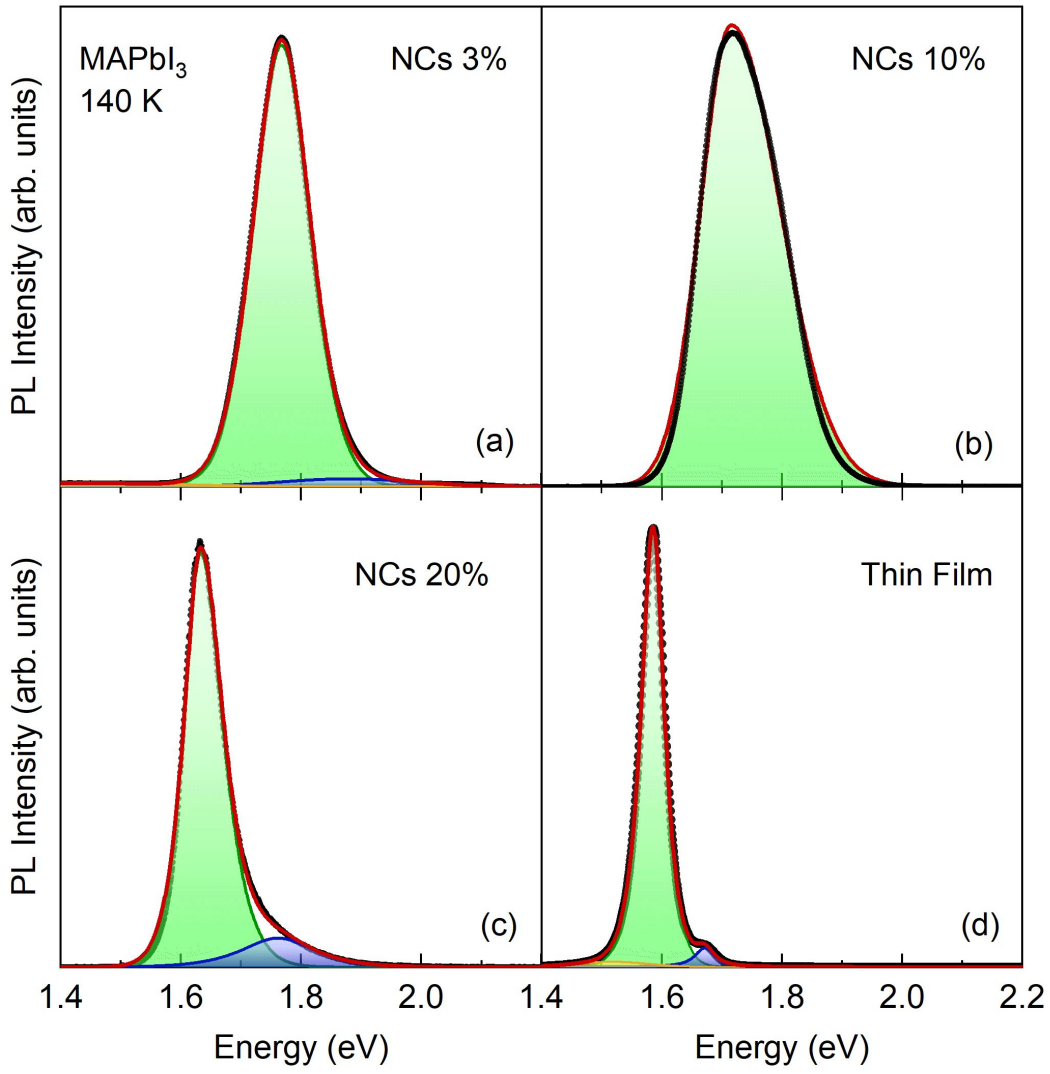

Figure S10: Representative PL spectra (black solid dots) measured at a temperature of 140 K for the $MAPbI_3$ NC samples with (a) 3 at% (NC diameter d=4 nm), (b) 10 at% (d=5 nm), and (c) 20 at% (d=8 nm) precursor concentrations and (d) the polycrystalline thin film. The red curves represent fits to the data points using a Gauss-Lorentz cross-product function (Equation S3). The green shaded peaks correspond to the free-exciton emission, whereas the blue-shaded ones are auxiliary peaks for improving the fitting.

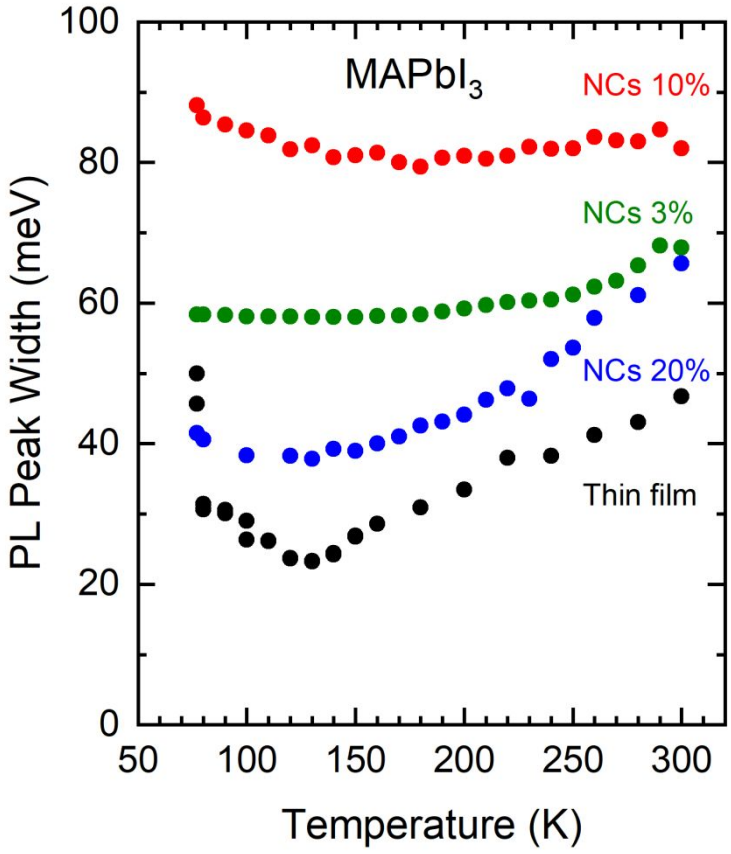

Figure S11: FWHM of the PL emission versus temperature (solid color symbols) for a polycrystalline $MAPbI_3$ film and samples with different nanocrystal sizes (NC diameter d=8 nm, 5 nm and 4 nm for 20%, 10% and 3% perovskite precursor concentration, respectively), as indicated.

Figure S11 shows the temperature dependence of the PL peak width, corresponding to the full width at half maximum (FWHM), for the thin film and samples with different NC sizes. The FWHM values were obtained from the line shape analysis of the PL spectra using the Gauss-Lorentz cross-product function given by Eq. (1). Typically, if an excitonic emission peak is *homogeneously* broadened, which means its width is inversely proportional to the exciton lifetime, the FWHM exhibits an exponential increase with increasing temperature [4,15]. This seems not to be the case for our $MAPbI_3$ NC samples, which for the smallest NC sizes the FWHM even results fairly temperature insensitive (see Fig. S11). We are thus lead to the conclusion that the PL peaks of the perovskite nanocrystal samples are *inhomogeneously* broadened, such that the FWHM simply reflects the polydispersity in NC size. In full agreement with this interpretation, we notice that the larger the absolute value of the FWHM, the less temperature sensitive is the PL width. This means, for example, that the sample with 10% precursor concentration exhibits the widest NC-size distribution of all samples.

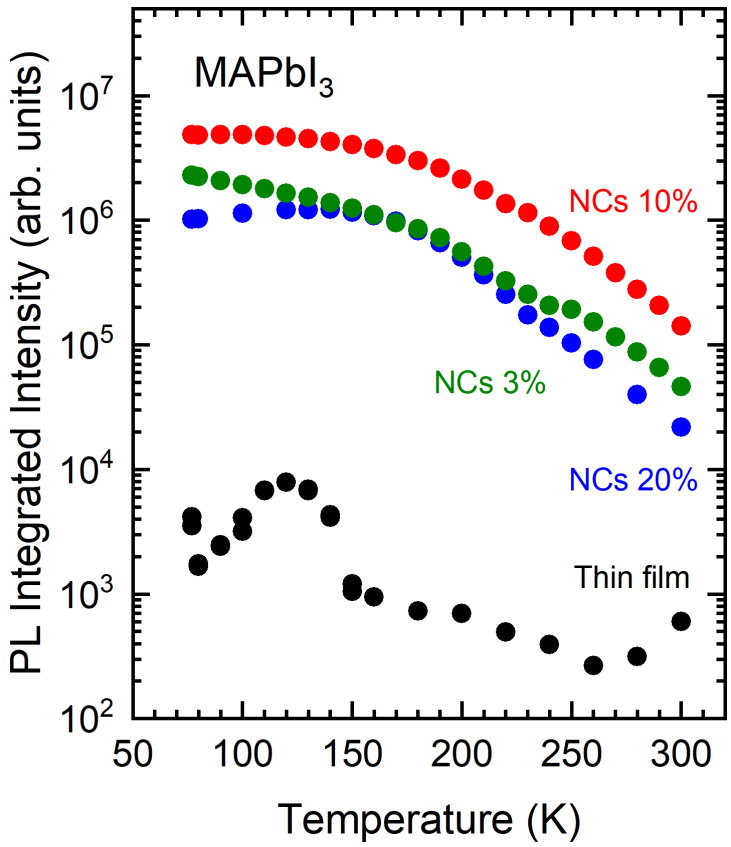

Figure S12: Temperature dependence of the integrated PL intensity for a perovskite thin film and $MAPbI_3$ nanocrystals prepared from solutions with different perovskite precursor concentrations, as indicated (NC diameter d=8 nm, 5 nm and 4 nm for 20%, 10% and 3% concentration, respectively).

The last aspect that we want to consider is the variation of PL intensity in the range of temperatures explored. In Fig. S12, we plot the integrated PL intensity as a function of temperature for the thin film and the NC samples. The integrated intensity is given by the product $Ax\Gamma$ of the amplitude times the width of the fitted Gauss-Lorentz cross-product function, corresponding to Eq. (1). In all cases, the PL intensity decreases with increasing temperature. This feature indicates that the PL emission is thermally activated (thermal quenching), behaviour which is described by the Arrhenius equation:

$$I(T) = \frac{I(0)}{1 + C * e^{\left(\frac{-E_a}{k_B T}\right)}} \qquad (2)$$

where *I(0)* represents the PL intensity at zero Kelvin, *C* is a fitting constant, k_B is the Boltzman constant and E_a represents the activation energy. Nevertheless, we refrain from extracting an activation energy from our data sets for the very fact that the structural situation regarding the progressive phase transformation from tetragonal to orthorhombic is not clear yet (see text in main manuscript for details).

Please note that we have refrained from performing the analysis of the temperature variation of FWHM and emission intensity in terms of electron-phonon interaction-driven broadening and thermally activated emission, respectively, for two reasons. First, the temperature range of our experiments is inadequate. The low upper bound of about 10 meV for the phonon frequencies of the modes typically leading to strong electron-phonon coupling [3,16] imply that substantial changes in the phonon populations only happen at very low temperatures below 50 K. Second, the uncertain structural behavior of the nanocrystalline perovskites with decreasing temperature forbids drawing conclusions about the evolution of PL line widths and peak intensities with temperature.

Pressure-dependent PL measurements

Figure S13 shows series of PL spectra recorded as a function of pressure for two different NC sizes (average diameters of 5 nm and 8 nm). With increasing pressure, the center position of the PL peak shifts slightly to lower energies, as accurately extracted by line shape fits using a Gaussian-Lorentzian cross product function.

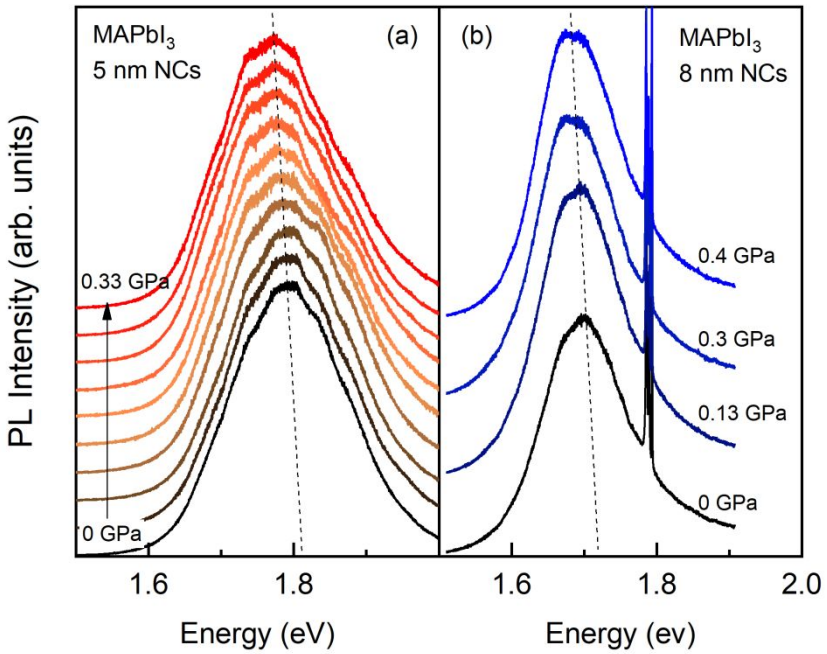

Figure S13: PL spectra of $MAPbI_3$ nanocrystals (NCs) with average diameter (a) of 5 nm and (b) 8 nm, recorded as a function of hydrostatic pressure.

Potentially relevant effects at T<240 K

Finally, we comment on the unusual temperature dependence of the gap observed at temperatures below 240 K for the NC samples, which develops a more or less

pronounced positive bowing depending on NC size (see Fig. 3 in the main body of the manuscript). A somewhat similar behavior of the gap has been recently observed for bulk mixed organic-cation $FA_xMA_{1-x}PbI_3$ crystals at intermediate compositions and temperatures lower than 250 K [4]. This behavior sets in when the perovskite transforms into a highly disordered tetragonal phase characterized by a large strain inhomogeneity. We speculate that in the case of the NCs there might be a strain inhomogeneity but of different origin. It is very plausible to consider that the small nanocrystals which form inside the pores of the amorphous silica matrix consist of a fairly ordered, single crystalline core and a disordered (non-homogeneously deformed) but crystalline shell. As the temperature decreases, the shell might provide seeding points for the orthorhombic phase, since the disorder in the shell also implies massive octahedral tilting and large strain inhomogeneity. In these seeding points, the transformation from tetragonal to orthorhombic phase can start at a higher temperature than in bulk due to the local strain, propagating inwards a certain level of disorder as the temperature decreases. Hence, because the surface-to-volume ratio increases with decreasing NC size, one would expect that smaller NCs begin to transform earlier than larger ones, as partially supported by XRD measurements. With decreasing temperature, the earlier the structural transition begins, the earlier the gap energy would start to level up, leading to the observed systematics in the temperature-induced gap renormalization, as shown in Fig. 3. Due to the analogous effects of thermal contraction and the application of compressive stress, our idea of an advanced temperature-induced phase transition for smaller NC sizes is supported by recent high-pressure experiments in $CsPbBr_3$ NCs [17]. A lower transition pressure is observed for Cs-based NCs, when the length scale of the octahedral tilting fluctuations, causing the structural phase transition, seems to approach NC sizes below 8 nm [17]. Finally, we point out that the structural uncertainties below 240 K mentioned above hamper the analysis of the different contributions form thermal expansion and electron-phonon interaction to the gap renormalization. For that analysis to make sense, it is imperative to pursue a systematic study of the pressure dependence of the gap but temperature by temperature. These experiments are currently under way.

References:

(1) Rubino, A.; Anaya, M.; Galisteo-López, J. F.; Rojas, T. C.; Calvo, M. E.; Míguez, H. Highly Efficient and Environmentally Stable Flexible Color Converters Based on Confined $CH_3NH_3PbBr_3$ Nanocrystals. *ACS Appl. Mater. Interfaces* **2018**, 10, 38334-38340.

(2) Lee, J.-H.; et al. Role of Hydrogen Bonding and its Interplay with Octahedral Tilting in $CH_3NH_3PbI_3$. *Chem. Commun.* **2015**, 51, 6434.

(3) Leguy, A. M. A.; Goñi, A. R.; Frost, J. M.; Skelton, J.; Brivio, F.; Rodríguez-Martínez, X.; Weber, O. J.; Pallipurath, A.; Alonso, M. I.; Campoy-Quiles, M.; Weller, M. T.; Nelson, J.; Walsh, A.; Barnes, P. R. F. Dynamic Disorder, Phonon Lifetimes, and the Assignment of Modes to the Vibrational Spectra of Methylammonium Lead Halide Perovskites. *Phys. Chem. Chem. Phys.* **2016**, 18, 27051-27066.

(4) Francisco López, A.; Charles, B.; Weber, O. J.; Alonso, M. I.; Garriga, M.; Campoy-Quiles, M.; Weller, M. T.; Goñi, A. R. Phase Diagram of Methylammonium/Formamidinium Lead Iodide Perovskite Solid Solutions from Temperature Dependent Photoluminescence and Raman Spectroscopies. *J. Phys. Chem. C* **2019**, 124, 3448-3458.

(5) Yu, P. Y.; Cardona, M. *Fundamentals of Semiconductors* **1995** (Springer, Berlin).

(6) Saba, M.; Cadelano, M.; Marongiu, D.; Chen, F.; Sarritzu, V.; Sestu, N.; Figus, C.; Aresti, M.; Piras, R.; Geddo Lehmann, A.; Cannas, C.; Musinu, A.; Quochi, F.; Mura, A.; Bongiovanni, G. Correlated Electron-hole Plasma in Organometal Perovskites. *Nat. Commun.* **2014**, 5, 5049-5058.

(7) Goñi, A. R.; Syassen, K. Optical Properties of Semiconductors Under Pressure. Semicond. Semimetals **1998**, 54, 247-425, and references therein.

(8) Klingshirn, C. F. *Semiconductor optics* **1997** (Springer, Berlin).

(9) Brus, L. E. Electron-Electron and Electron-Hole Interactions in Small Semiconductor Crystallites: The Size Dependence of the Lowest Excited Electronic State. *J. Chem. Phys.* **1984**, 80, 4403-4409.

(10) Anaya, M.; Rubino, A.; Rojas, T.C.; Galisteo-López, J.F.; Calvo, M.E.; Míguez, H. Strong Quantum Confinement and Fast Photoemission Activation in $CH_3NH_3PbI_3$ Perovskite Nanocrystals Grown within Periodically Mesostructured Films. *Adv. Opt. Mater.* **2017**, 5, 1601087

(11) Yang, Z.; Surrente, A.; Galkowski, K.; Bruyant, N.; Maude, D. K.; Haghighirad, A. A.; Snaith, H. J.; Plochocka, P.; Nicholas, R. J. Unraveling the Exciton Binding Energy and the Dielectric Constant in Single-Crystal Methylammonium Lead Triiodide Perovskite. *J. Phys. Chem. Lett.* **2017**, 8, 1851– 1855

(12) Mao, H.-K.; Xu, J.; Bell, P. M. Calibration of the Ruby Pressure Gauge to 800 kbar under Quasi-Hydrostatic Conditions. J. Geophys. Res.1986, 91, 4673-4676.

(13) Francisco López, A.; Charles, B.; Weber, O. J.; Alonso, M. I.; Garriga, M.; Campoy-Quiles, M.; Weller, M. T.; Goñi, A. R. Pressure-Induced Locking of Methylammonium Cations Versus Amorphization in Hybrid Lead Iodide Perovskites. J. Phys. Chem. C **2018**, 122, 22073-22082.

(14) Wojdyr, M. Fityk: A General-Purpose Peak Fitting Program. *J. Appl. Crystallogr.* **2010**, 43, 1126-1128.

(15) Wright, A. D.; Verdi, C.; Milot, R. L.; Eperon, G. E.; Pérez-Osorio, M. A.; Snaith, H. J.; Giustino, F.; Johnston, M. B.; Herz, L. M. Electron-Phonon Coupling in Hybrid Lead Halide Perovskites. *Nature Commun.* **2016**, 7, 11755/1-9.

(16) Francisco López, A.; Charles, B.; Weber, O. J.; Alonso, M. I.; Garriga, M.; Campoy-Quiles, M.; Weller, M. T.; Goñi, A. R. Equal Footing of Thermal Expansion and Electron-Phonon Interaction in the Temperature Dependence of Lead Halide Perovskite Band Gaps. *J. Phys. Chem. Lett.* **2019**, 10, 2971-2977.

(17) Beimborn II, J. C.; Walther, L. R.; Wilson, K. D.; Weber, J. M. Size-Dependent Pressure-Response of the Photoluminescence of CsPbBr3 Nanocrystals. *J. Phys. Chem. Lett.* **2020**, 11, 1975-1980.